Ultramicroscopy 30 (1989) 58–69
North-Holland, Amsterdam

Z-CONTRAST STEM FOR MATERIALS SCIENCE

S.J. PENNYCOOK

Solid State Division, Oak Ridge National Laboratory, Oak Ridge, Tennessee 37831-6024, USA

Received at Editorial Office 6 December 1988; presented at Symposia August 1988

The use of a high-angle annular detector on a scanning transmission electron microscope (STEM) for imaging crystalline materials with strong chemical sensitivity is described. The image can be used to form an elemental map with high efficiency which can be quantified directly in terms of atomic concentrations. Examples of ion-implanted silicon recrystallized by solid- or liquid-phase epitaxial growth will be shown, illustrating the usefulness of the image in studies of phase transformations and grain boundary segregation. At high resolution it is possible to resolve a crystal lattice, while preserving the strong chemical sensitivity of the image. A simply interpretable image results, with a minimum dependence on objective lens defocus and specimen thickness, and examples of high-temperature superconductors will be shown.

1. Introduction

Z-contrast methods using a scanning transmission electron microscope (STEM) were introduced many years ago by Crewe and co-workers in their pioneering work on the imaging of single heavy atoms supported on thin carbon films [1,2]. They realized that an annular detector arranged to collect electrons scattered outside the incident beam cone would collect a large fraction of the total elastically scattered flux and therefore provide the most efficient imaging mode for beam-sensitive materials, coupled with strong atomic number or Z contrast characteristic of the total elastic scattering cross-section (approximately a $Z^{3/2}$ dependence). They also realized that an axial electron spectrometer could be used to detect a large fraction of the total inelastic scattering which for small thicknesses gave a signal proportional to thickness and showing only weak Z contrast (approximately a $Z^{1/2}$ dependence). A ratio of the annular detector signal to the axial electron loss signal resulted in impressive images in which the contrast due to thickness variations in the carbon film was greatly reduced and single heavy atoms were clearly visible with contrast proportional approximately to Z. Isaacson et al. further demonstrated that Pd and Pt atoms could be distinguished in the Z-contrast image from their spot intensities [3].

Apart from a study of surface diffusion [4] for many years the Z-contrast methods found application almost exclusively in the biological sciences [5–7], where the STEM certainly enjoys a considerable advantage over conventional TEM for the efficient imaging of beam-sensitive materials with high contrast. For materials science studies, although we are less concerned with imaging efficiency, the availability of an image showing strong Z contrast would also be extremely useful for many applications. There has indeed been a consistent effort to improve the sensitivity of conventional imaging to impurity atoms and clusters, using high-resolution bright field imaging, tilted dark field or diffuse imaging [8–12] but the STEM Z-contrast method in its original form fails with the crystalline samples almost invariably encountered in materials science problems. The low-angle scattering from crystals no longer follows the simple form of a single atom but is dominated by diffraction effects, with the result that an annular detector which collects these diffracted beams will give an image similar to dark field conventional TEM images. The diffraction contrast effectively obscures any Z contrast which may be present and makes a simple chemical interpretation of the

0304-3991/89/$03.50 © Elsevier Science Publishers B.V.
(North-Holland Physics Publishing Division)

image impossible [13]. The inelastic signal preserves to a large extent the diffraction contrast of the bright field image, and is therefore largely complementary to the annular detector contrast. Forming a ratio as before only increases diffraction contrast effects.

To retrieve the Z contrast these diffracted electrons must be excluded from contributing to the image, for example by using an annular detector with a large inner collection angle as suggested by Howie [14]. Electrons scattered at high angles necessarily suffer small impact parameters with the atomic nuclei in the specimen. At angles of 50 or 100 mrad at 100 keV the impact parameters are 0.012 or 0.006 nm, respectively, less than typical atomic vibration amplitudes, so that the material scatters as an incoherent assembly of atoms, diffraction contrast is lost, and Z contrast returns. In fact, defining small impact parameters in this way ensures that the scattering is largely unscreened and the cross-section approaches the very strong Z^2 dependence of Rutherford scattering. Again, forming a ratio with the inelastic signal is undesirable unless it also can be obtained over a similar angular range [15], in which case contrast due to thickness variations could be reduced and the image contrast would again be proportional to Z.

The high-angle detector signals will still be sensitive to crystal orientation through the electron channeling phenomenon. Although diffracted beams are not detected after they emerge from the crystal, in an orientation giving strong dynamical diffraction, their effect inside the crystal causes the electron flux to be concentrated on or between the atomic planes or strings, and the yield of high-angle elastically or inelastically scattered electrons will be altered proportionately. Under these conditions, defects will be visible again, since locally they will alter the channeling effect [16,17].

The first applications of the high-angle annular detector were with catalyst samples consisting of small heavy clusters supported on light amorphous or polycrystalline supports [18–21]. The Z-contrast image greatly improved the visibility of the clusters, particularly on crystalline supports. For the smallest clusters, considerable quantitative information on particle sizes can be extracted from such images which is unavailable from the bright field phase contrast image [22]. In this paper we concentrate on applications in materials science in which the sample can be tilted either into or away from specific crystallographic directions. For the first part of the paper we show how the Z-contrast image can be used as a quantitative elemental map obtained with the efficiency characteristic of an image, many orders of magnitude higher than spectroscopic techniques. A number of examples will be shown of the recrystallization of silicon following ion implantation with heavy dopants, where precipitation and segregation of the dopant controls the recrystallization. Z-contrast imaging allows these phenomena to be studied by providing a high-contrast image independent of the phase of the silicon. In the second part of the paper we consider the available resolution of the technique, and show how it is possible to resolve a crystal lattice while preserving the strong chemical sensitivity characteristic of high-angle elastic scattering, showing examples of high-temperature superconductors. The image is only weakly dependent on sample thickness and objective lens defocus, parameters which dominate the contrast in a conventional phase-contrast high-resolution image, and promises to be of great value as a complementary high-resolution imaging technique.

2. Quantitative elemental mapping

Fig. 1 demonstrates very clearly the change in the information content of the image between low-angle and high-angle electron scattering. Cross-section images of Si(100) implanted with Sb^+ (80 keV, 1.5×10^{16} cm^{-2}) and recrystallized by solid-phase epitaxial (SPE) growth at 550 °C for 40 min were taken in a Philips EM 400T operating at 100 keV with a LaB_6 filament [23]. The conventional bright-field image (fig. 1a) shows how at this high Sb concentration the regrowth broke down approximately 30 nm from the surface to give a high density of twins for the remainder of the growth. A band of defects marking the original amorphous/crystalline interface is also visible. Fig. 1b shows the annular dark-field image under the same diffraction conditions, with the Bragg beams reaching the detector. It is simply a

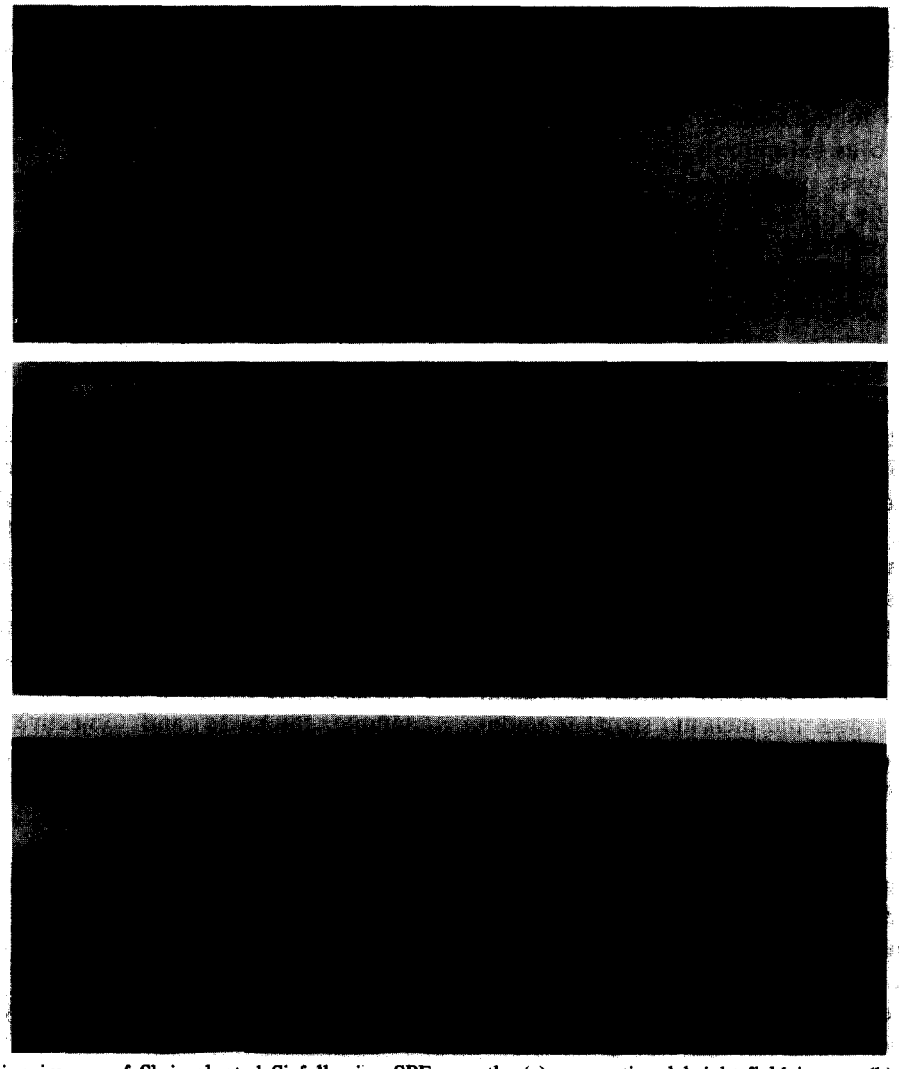

Fig. 1. Cross-section images of Sb-implanted Si following SPE growth: (a) conventional bright-field image; (b) STEM low-angle annular dark-field image showing diffraction contrast; (c) STEM high-angle annular dark-field image showing Sb distribution via Z contrast.

dark-field image dominated by diffraction contrast showing the defects present in the material but giving no direct information on the dopant which induced the defects. By increasing the inner detector angle to 65 mrad, and tilting away from the two-beam condition to avoid channeling effects, all contrast due to defects is removed, and the Sb distribution becomes directly visible through the Z-contrast mechanism (fig. 1c). The Gaussian profile of the original implant is clearly visible and a narrow band of high concentration marks the onset of twin formation.

The image in this form can be directly interpreted as an elemental map. Since the sample is fairly uniform in thickness, and there are no strong electron channeling effects, the image contrast C,

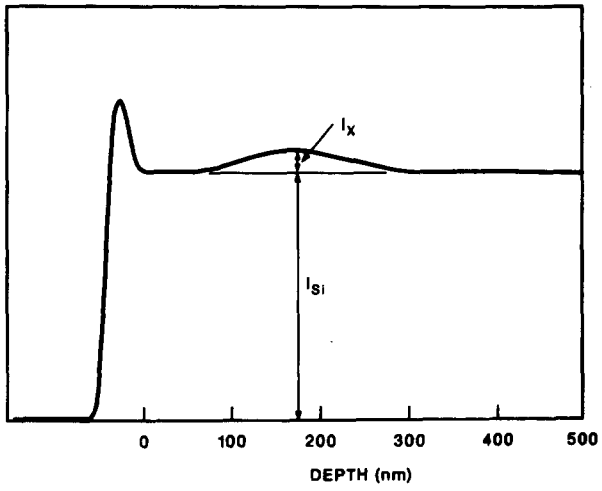

Fig. 2. Line trace across Z-contrast image of Bi-implanted Si following SPE growth, defining image contrast $C = I_x/I_{Si}$.

defined as the additional signal in the highly doped region divided by the signal due to the undoped Si (see fig. 2), is linearly proportional to dopant concentration c_x:

$$C = \left(\frac{\sigma_x}{\sigma_{Si}} - F_s\right) c_x, \tag{1}$$

where σ_x and σ_{Si} are the cross-sections for scattering into the high-angle detector for the dopant and Si, respectively. F_s is the substitutional fraction of the dopant which takes account of the fact that for every dopant atom introduced F_s silicon atoms are removed. F_s can be obtained from bulk ion channeling analysis or from local electron channeling analysis. For the heavier dopants it becomes a small correction and need not be known to a high accuracy. To achieve a standardless analysis, we need to find reliable expressions for the cross-sections. In the angular range we are concerned with, the scattering is significantly reduced from that predicted by the unscreened Rutherford cross-section. We have studied the accuracy of a number of cross-section expressions over a wide range of Z and a wide range of inner detector angles using standard samples of known concentrations [17]. Fig. 3 shows a comparison of experimental data for Bi-implanted Si compared to a number of cross-section expressions. The vertical axis

$$\eta = \frac{\sigma_{Bi}}{\sigma_{Si}} \frac{Z_{Si}^2}{Z_{Bi}^2}$$

is the cross-section ratio with the Rutherford Z^2 dependence removed. For unscreened scattering the experimental points would lie along the line $\eta = 1$, which is clearly not the case, indicating significant screening remains. The Born approximations fail to account adequately for screening in this angular range, being almost a factor of two in error. The popular tabulated scattering factors of Doyle and Turner [24] also fail in this regime, since they also are based on the Born approximation. The best overall fit was obtained for an expression due to Fleischmann [25] which although overestimating η somewhat was consistently closest to the experimental points. His expression gives

$$\sigma_x \propto Z_x^2 \left(\frac{\theta_2 - \theta_1}{\theta_1 \theta_2 \theta_\alpha'} + \frac{1}{\theta_\alpha'^2} \ln \frac{\theta_1(\theta_2 + \theta_\alpha')}{\theta_2(\theta_1 + \theta_\alpha')} \right). \tag{2}$$

where

$$\theta_\alpha'^2 = e\theta_0^2(1.13 + 3.76\alpha^2), \tag{3}$$

$$\alpha = Z/137\beta, \tag{4}$$

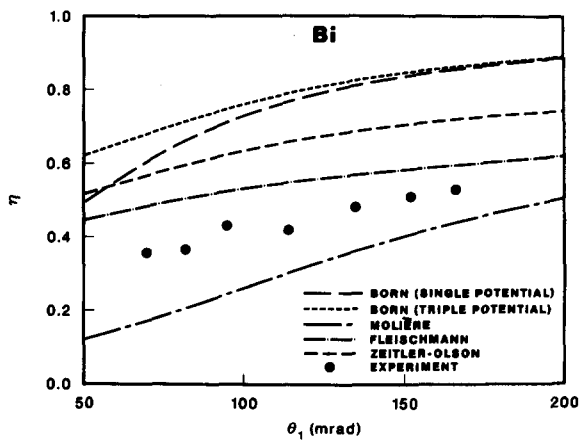

Fig. 3. Experimental values of η as a function of inner detector angle for Bi in Si determined from standard sample, compared to various theoretical predictions (outer detector angle = 275 mrad).

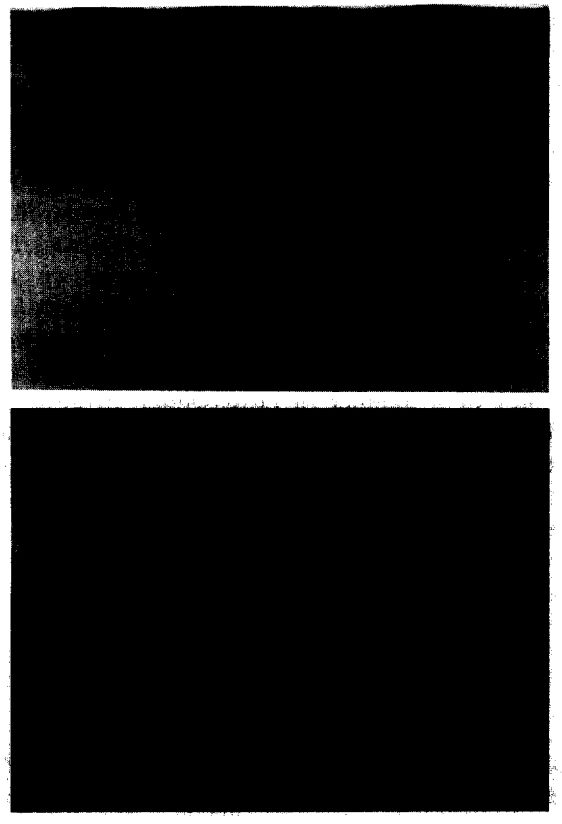

Fig. 4. Cross-section of Sb-implanted silicon after pulsed laser annealing: (a) conventional diffraction contrast image; (b) Z-contrast STEM image of Sb distribution.

$e = 2.7183$, and θ_1 and θ_2 are the inner and outer detector angles. θ_0 is the Born screening angle given by

$$\theta_0 = 1.13Z^{1/3}/137\beta, \quad (5)$$

where $\beta = v/c$ the ratio of the electron velocity to the velocity of light.

An example of a quantitative analysis is shown in fig. 4. A sample of Si(100) implanted with Sb (150 keV, 4×10^{16} cm^{-1}) was recrystallized by liquid-phase epitaxial growth using a pulsed KrF excimer laser (energy density 1.0 J cm^{-2}) [26]. A cell structure resulted, shown clearly in the conventional bright field cross-section image (fig. 4a). The Z-contrast image taken on a VG Microscopes HB501A STEM using the normal high-excitation pole piece is shown in fig. 4b, and shows not only the cell structure, but the Sb in solution between and below the cells. The concentration is seen to be remarkably uniform laterally between the cells and decreasing from the peak of the implant towards the surface, indicating a slow-down of the melt front. The bright-field image in this region is dominated by strain contrast and could not be interpreted simply in terms of Sb concentration. A line scan between the cells gave a peak concentration of 2.0×10^{21} cm^{-3} using an experimentally determined cross-section ratio, an order of magnitude above the equilibrium retrograde maximum solubility limit.

A more complicated situation is shown in fig. 5. This is an attempt to recrystallize Si(100) implanted with In (125 keV, 2×10^{-15} cm^{-2}) by rapid thermal annealing at 700 °C for 60 s. SPE growth has proceeded halfway through the implant profile while the near-surface region has turned to a fine-grain polycrystalline material, shown by the bright-field TEM image (fig. 5a). The Z-contrast image, also taken on a VG Microscopes HB501A, clearly shows In precipitates not only in the recrystallized Si but also in the polycrystalline Si, as well as a high concentration of precipitates and of In in solution just ahead of the advancing SPE growth front. Gross changes in the In concentration profile accompany both the SPE growth and the amorphous-to-polycrystalline transformation, which can proceed in regions of high In concentration independent of the SPE growth front [27,28]. Z-contrast STEM of a sample just beginning to transform has shown clearly the presence of In precipitates in a largely amorphous matrix [29]. The In precipitation occurs in the amorphous silicon, and is characterized by a concentration-dependent diffusion coefficient many orders of magnitude enhanced over crystalline tracer values. Interestingly, In precipitation in crystalline silicon is also enhanced to a similar degree, suggesting that diffusion in crystalline and amorphous silicon is essentially similar. The microstructure in fig. 5 can now be understood as follows. The In precipitates are liquid at all practical annealing temperatures, and since Si has a small solubility in liquid In (of the order of 1 at%) the droplets will be highly mobile in response to a driving force [30]. Suppose heterogeneous nucleation of crystalline silicon took place in the inside

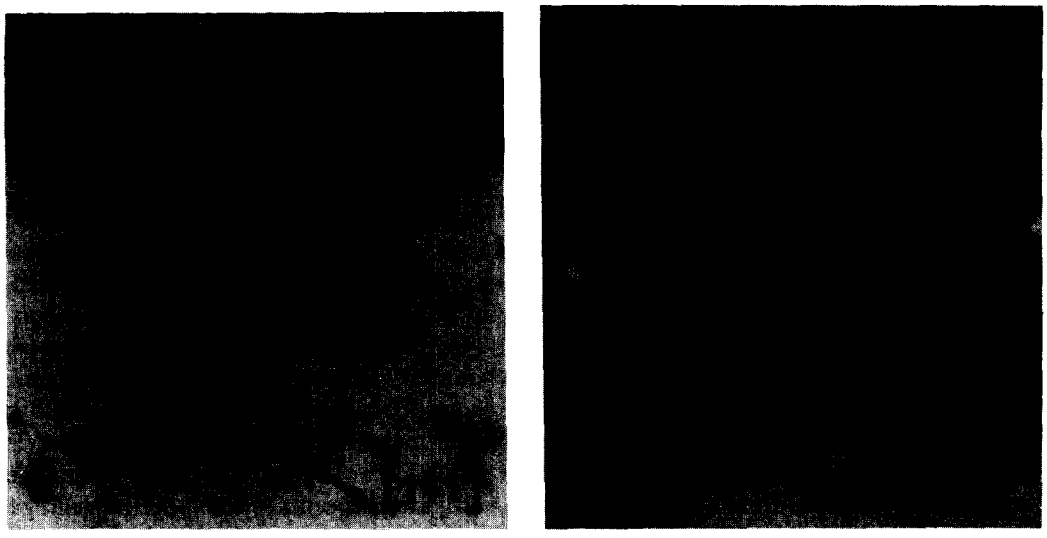

Fig. 5. High-dose In-implanted Si after rapid thermal annealing: (a) conventional diffraction contrast image showing end-of-range damage, In precipitates in crystalline Si, and a fine-grained polycrystalline region; (b) Z-contrast STEM image showing In precipitates in the crystalline and polycrystalline regions, and pile-up of precipitates and In in solution ahead of the crystallization front.

curved surface of the liquid droplet (a geometry which could greatly enhance nucleation rates compared to heterogeneous nucleation at a flat interface [31]); then there would be a very large Si flux available from the liquid In compared to the flux available from the solid amorphous silicon, even if solid-state diffusion was enhanced several orders of magnitude. To replace the flux lost to the growing crystal amorphous silicon would dissolve into the In droplet, and so growth of the crystal-

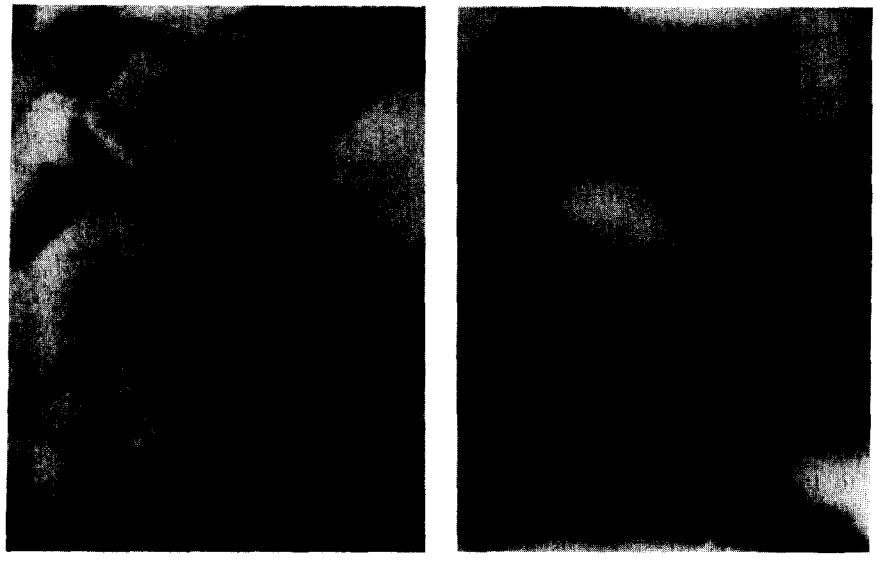

Fig. 6. Polycrystalline Si implanted with As and furnace-annealed: (a) bright-field STEM image showing diffraction contrast; (b) Z-contrast STEM image showing As segregation at grain boundaries.

lite naturally results in droplet migration, explaining the long-range In redistribution always seen on the amorphous-to-polycrystalline transformation. The driving force is effectively the full free energy of transformation, and simple estimates of the resultant velocities indicate transformation rates at least as high as observed experimentally [31]. The pileup of precipitates ahead of the SPE growth front in fig. 5b can also be explained since it requires surface energy to incorporate a droplet into the crystalline phase. An advancing SPE growth front will be able to sweep up droplets ahead of or at the crystalline interface, until heterogeneous nucleation of crystalline silicon has occurred in a sufficient fraction of the droplets to halt the epitaxial recrystallization. The high In concentration in solution ahead of the interface is expected due to the higher solubility of In in amorphous Si compared to crystalline Si.

Another area where the availability of a sensitive analytical image is of great advantage is that of grain boundary segregation. Fig. 6 shows images of polycrystalline Si grown on Si(100) by chemical vapor deposition, followed by implantation with As (40 keV, 1×10^{16} cm^{-2}) and annealing at 950 °C for 25 min [33]. This is a typical procedure used to form the emitter region and contact in bipolar Si technology. For microscopy, the columnar form of polycrystalline material grown this way is very convenient, resulting in many boundaries nearly vertical in a plan-view sample, and the geometry is largely preserved during implantation and recrystallization. It is known from electrical measurements that As segregates to the grain boundaries, where it diffuses through the polycrystalline layer to dope the single crystal substrate. This segregation is clearly visible in the Z-contrast image (fig. 6b) showing as bright lines at most of the grain boundaries. The contrast is not dependent on the diffraction conditions of the neighboring grains, indicating electron channeling effects to be unimportant. The strongly diffracting grain in the center of the image shows boundary contrast similar to that of nondiffracting grains, although twins in the center of the grain are visible through channeling contrast as discussed earlier. A line scan across the boundaries can quantify the segregation, in the same way as can be done using X-ray fluorescence, except that the data can be obtained and displayed in real time. Beam-broadening considerations are essentially identical for both signals, and are limiting the resolution in the Z-contrast image of fig. 6b, which was taken using a VG HB501 STEM equipped with an ultrahigh-resolution pole piece. From line scans across several boundaries, the As concentration was typically 1–2 at% in the analyzed volume, in good agreement with previous X-ray studies [34]. If the As is assumed segregated at the boundary plane its concentration would be an order of magnitude higher, which could be tested experimentally using thinner specimens. The availability of an image is a great advantage for investigating the uniformity of the segregation, although in this material all boundaries appeared to be segregated to approximately the same level, those not showing segregation being those not vertical in the image. Changes in segregation at different boundary types or at defects could be simply investigated, and an image always allows the possibility of unpredicted effects showing up. In multicomponent systems the Z-contrast image should be just as useful, although its interpretation may require some representative X-ray spectra to be taken.

3. High resolution Z-contrast imaging of crystals

Incoherent imaging intrinsically has a 30% better resolution limit than coherent phase contrast imaging using the same accelerating voltage and objective lens spherical aberation C_s, as shown originally by Scherzer [35]. The point-to-point image resolution is given by $d_{min} = 0.43\ C_s^{1/4}\lambda^{3/4}$, compared to the 0.66 prefactor for coherent imaging, so that with a high-angle annular detector on a high-resolution STEM it should be possible to both resolve a crystal lattice and preserve the strong chemical sensitivity of the Z-contrast image. To test this possibility a VG Microscopes HB501 STEM was acquired, equipped with a new ultrahigh-resolution pole piece having a theoretical C_s of 1.3 mm and a ±10° double-tilt specimen holder. This gives a theoretical image resolution at 100 keV of 0.22 nm, which is obtained using the

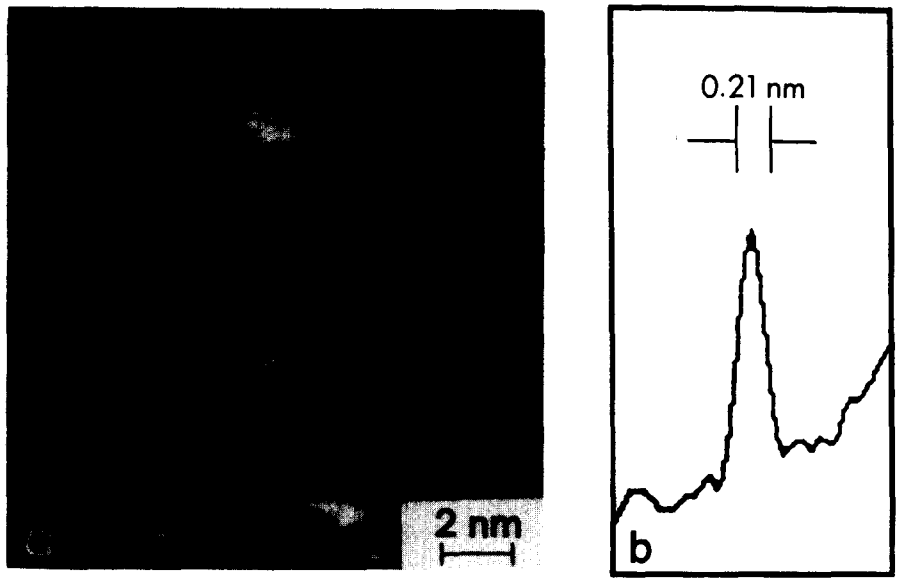

Fig. 7. (a) STEM image of uranium clusters on a thin carbon film, smallest spots are individual atoms; (b) intensity profile across single atom.

optimum illuminating aperture, semiangle $\alpha_0 = (4\lambda/C_s)^{1/4}$, and at the optimum defocus $\delta_o = -(\lambda C_s)^{1/2}$. Under these conditions the probe intensity profile is very close to that of an Airy disc and has a full width half maximum (FWHM) very close to d_{min} [35–40]. It should be emphasized that this is the limiting point-to-point image resolution, whereas for analytical purposes the probe size is sometimes defined differently [41]. This high-resolution configuration should also be compatible with conventional X-ray microanalysis, with an expected solid angle of collection of 0.17 sr.

The best experimental test of the incoherent resolution limit is to image a point scatterer when the image profile is just the profile of the probe. Fig. 7a shows an image of single uranium atoms supported on a thin carbon film, clearly showing small bright spots in the expected size range. The image was obtained with $\alpha = 11.4$ mrad (50 μm objective aperture) close to the optimum $\alpha_o = 10.3$ mrad, and collecting electrons scattered over approximately 15–150 mrad for high efficiency. The estimated geometrical size of the probe on the specimen was less than 0.05 nm. Fig. 7b shows an intensity profile across a single atom taken in the direction of the line scan, indicating a probe FWHM of 0.21 nm. Profiles typically gave FWHM in the region 0.21 to 0.24 nm, indicating a performance in excellent agreement with the theoretical prediction.

We should therefore be in a good position to test Z-contrast imaging of crystal lattices having spacings greater than this resolution limit. Perfect test samples are provided by the high-temperature superconducting oxides, in which elements of widely different Z are present on well separated planes. Fig. 8a shows a cross-section Z-contrast image of $YBa_2Cu_3O_{7-x}$ single crystal viewed normal to the c-axis clearly showing the triplet perovskite cell structure, the two bright lines corresponding to the planes containing the Ba ($Z = 56$) and the less bright one between them corresponding to the Y plane ($Z = 39$). The inner collection angle of the annular detector has now been increased to 50 mrad semiangle by using a mask. Fig. 8b shows the image from the rare-earth substituted material $ErBa_2Cu_3O_{7-x}$, where now the Er ($Z = 68$) plane is the brightest in the cell. Clearly it is possible to resolve a crystal lattice in the incoherent image and retain strong chemical sensitivity [42]. Quantitation of the image is no

longer expected to be simple since the beam is incident along a crystallographic direction, and electron channeling effects will alter the distribution of flux across the unit cell. Nevertheless, a simple calculation of the scattering power per plane using eq. (2) convoluted with an appropriate probe size does quite reasonably reproduce the relative intensities of the various planes, as shown in fig. 8. Such a calculation is analogous to the phase grating approximation in conventional phase-contrast imaging. Certainly it would be desirable to include dynamical diffraction effects explicitly [43] but the simple calculation holds significantly beyond the thickness at which the phase grating approximation fails in conventional imaging. There are two reasons for this. Firstly, the major effect of electron channeling is to concentrate the flux onto the atomic planes, the difference in the flux enhancements on the various planes within the unit cell building up as a second-order effect. Secondly, the incoherent image is formed from the integrated scattering through the whole thickness of the specimen, whereas the conventional phase contrast high-resolution image is formed by combining the diffracted beams emerging from the sample. Their relative phase, and hence the image contrast, depends very strongly on sample thickness through the Pendellösung effect, and very strongly on objective lens defocus, so that contrast due to chemical species can easily be obscured and extensive image simulation is needed to understand the imaging process. The Z-contrast image changes form slowly and smoothly with specimen thickness, generally tending to lose contrast with increasing thickness due to beam broadening. (Note, however, that under channeling conditions beam broadening is reduced markedly from the $t^{3/2}$ dependence for random incidence to a $t^{1/2}$ dependence [44].) It is also considerably less sensitive to objective lens

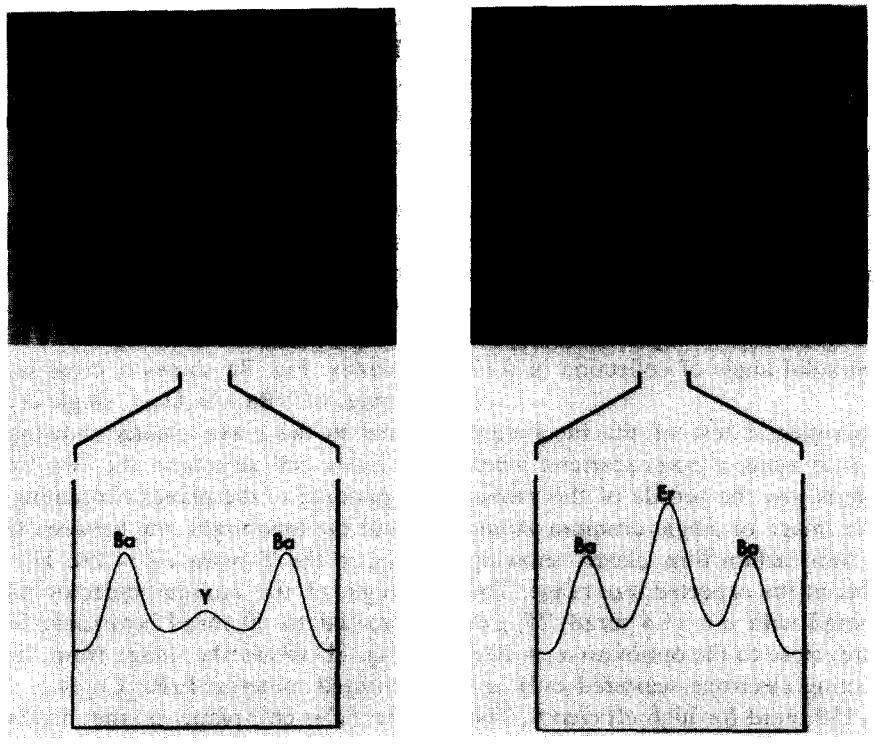

Fig. 8. High-resolution Z-contrast image from (a) $YBa_2Cu_3O_{7-x}$ and (b) $ErBa_2Cu_3O_{7-x}$ single crystals ($\alpha = 5.7$ mrad, $\beta = 50$–150 mrad). Line traces are calculated image intensity across the respective 1.19 nm unit cell in the c-direction assuming a Gaussian probe of 0.24 nm FWHM.

defocus. Changing the defocus changes the profile of the incident probe, but due to the strong electron channeling phenomenon the image is remarkably insensitive to the exact probe shape over a large range of defocus. In the incoherent image there are no contrast reversals with objective lens defocus.

However, one must be aware that electron channeling effects are strong, and match the incident beam divergence to the crystal spacing being imaged. Electrons incident at less than the Bragg angle θ_B for the required spacing tend to be channeled along the planes and enhance the Z-contrast. Electrons incident outside the Bragg angle will tend to be channeled between the planes and reduce the Z contrast. The channeling effect can easily be monitored using selected-area diffraction in the STEM, when the high-angle annular detector forms a channeling effect map [45] showing the incident beam directions resulting in enhanced high-angle scattering. For Si it was found that all angles from θ_B to $-\theta_B$ resulted in a similar enhancement which suggests that for Z contrast structure imaging the incident beam semiangle α should be chosen less than θ_B. The images in fig. 8 were taken using $\alpha = 5.7$ mrad, which is slightly larger than $\theta_B = 4.8$ mrad, corresponding to the basic 0.39 nm perovskite cell. Most of the flux will still be channeled along the heavy planes, but this is not the case if using the larger aperture $\alpha = 11.4$ mrad which was used for the single-atom imaging. This aperture results in a weak reversed contrast (fig. 9), since a large fraction of the incident beam is now incident outside the Bragg angle and tends to avoid the heavy planes.

Another advantage of the Z-contrast method is the highly localized nature of the imaging, defined by the physics of the scattering. For a conventional phase-contrast image, whether information from one specimen region is imaged locally depends on the transfer properties of the objective lens and is therefore not independent of the image contrast. For imaging defects and interfaces the incoherent signal guarantees a localized image, which together with the strong chemical sensitivity is expected to be of considerable advantage. As an example, fig. 10 shows a planar defect in the

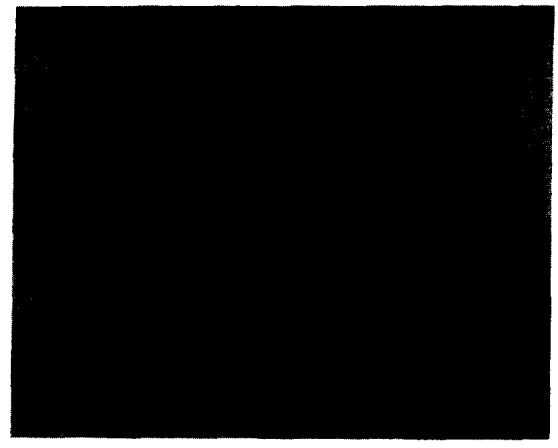

Fig. 9. Z-contrast image of $YBa_2Cu_3O_{7-x}$ resulting from a larger incident beam convergence ($\alpha = 11.4$ mrad).

$YBa_2Cu_3O_{7-x}$ single crystal. Although the Y planes are unresolved in this image, the defect is unambiguously seen to lie between the twin Ba planes in the unit cell. Near the top of the figure it expands the Ba planes by a distance $c/6$. This region can be seen easily by viewing along the planes at a low angle. The dark contrast indicates

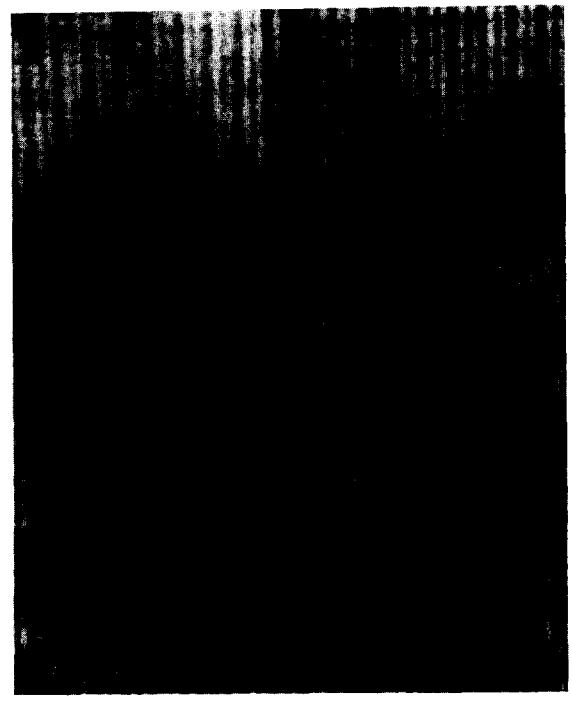

Fig. 10. Planar defect in $YBa_2Cu_3O_{7-x}$ single crystal.

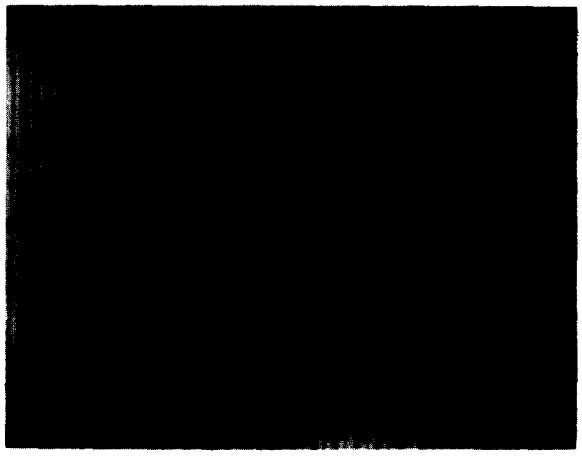

Fig. 11. Image from $YBa_2Cu_3O_{7-x}$ single crystal after significant degradation.

an atom of low Z so that the defect structure immediately suggested from the image consists of one additional Cu/O layer inserted between the Ba planes. This structure has also been proposed from conventional phase-contrast imaging, using microscopes of higher voltage and resolution, and interpreted to be either the response of the material to oxygen substoichiometry [46] or to result from a degradation reaction [47]. We favor the first interpretation and believe the lower region of the defect in fig. 10, where dark contrast is seen but no $c/6$ expansion, results from degradation. On leaving the sample several weeks in a desiccator it was found to have undergone considerable degradation as shown in fig. 11. The small defect and the lowest portion of the large defect again show dark contrast between the Ba planes but with no $c/6$ expansion. The image suggests that degradation proceeds by the outdiffusion, first of Cu then of Ba, to the sample surfaces, accompanied by the indiffusion of lighter species, most probably C and O.

4. Conclusion

Z-contrast imaging using a high-angle annular detector on a STEM provides an image with strong chemical sensitivity, which effectively bridges the gap between conventional imaging techniques and the low-intensity signals of conventional analytical electron microscopy. It can be used to provide a highly efficient elemental map or linetrace, which can be directly quantified using standard samples or using appropriate calculated crosssections. Alternatively it can be used as a high-resolution imaging technique, resolving a crystal lattice with strong chemical sensitivity but minimum dependence on microscope defocus or specimen thickness. Either way it is very complementary to conventional imaging and analysis techniques and will find many applications in materials science.

Acknowledgments

It is a pleasure to thank S.D. Berger and R.J. Culbertson for research collaborations, M.M.J. Treacy for loan of the uranium atoms, L.A. Boatner for providing single crystal superconductors, J.T. Luck and C.W. Boggs for technical assistance, and VG Microscopes for design of the ultrahigh-resolution pole piece. This research was sponsored by the Division of Materials Sciences, US Department of Energy, under contract No. DE-AC05-84OR21400 with Martin Marietta Energy Systems, Inc.

References

[1] A.V. Crewe and J. Wall, J. Mol. Biol. 48 (1970) 375.
[2] A.V. Crewe, J.P. Langmore, and M.S. Isaacson, in: Physical Aspects of Electron Microscopy and Microbeam Analysis, Eds. B.M. Siegel and D.R. Beaman (Wiley, New York, 1975) p. 47.
[3] M.S. Isaacson, D. Kopf, M. Ohtsuki and M. Utlaut, Ultramicroscopy 4 (1979) 101.
[4] M.S. Isaacson, J. Langmore, N.W. Parker, D. Kopf and M. Utlaut, Ultramicroscopy 1 (1976) 359.
[5] A. Engel, Ultramicroscopy 3 (1978) 273.
[6] C. Mory, C. Colliex, B. Revet and E. Delain, Ultramicroscopy 7 (1981) 161.
[7] K.L. Monson, J.S. Wall and J. Hainfield, Ultramicroscopy 21 (1987) 147.
[8] P.M. Fields and J.M. Cowley, Acta Cryst. A34 (1978) 103.
[9] L.A. Bursill and Shen Guan Jun, Optik 66 (1984) 251.
[10] N.D. Zakharov, M. Pasemann and V.N. Rozhanski, Phys. Status Solidi (a) 71 (1982) 275.
[11] R.W. Glaisher and A.E.C. Spargo, in: Electron Microscopy and Analysis 1983, Inst. Phys. Conf. Ser. 68, Ed. P. Doig (Inst. Phys., London–Bristol, 1984) p. 185.

[12] J.H. Rose and R. Gronsky, Mater. Res. Soc. Symp. Proc. 62 (1986) 57.
[13] A. Donald and A.J. Craven, Phil. Mag. A39 (1980) 1.
[14] A. Howie, J. Microscopy 117 (1979) 11.
[15] A.V. Jones, in: Proc. 46th Annual EMSA Meeting, Milwaukee, WI, 1988, Ed. G.W. Bailey (San Francisco Press, San Francisco, 1988) p. 648.
[16] M.M.J. Treacy and J.M. Gibson, in: Electron Microscopy and Analysis 1981, Inst. Phys. Conf. Ser. 61, Ed. M.J. Goringe (Inst. Phys., London–Bristol, 1982) p. 263.
[17] S.J. Pennycook, S.D. Berger and R.J. Culbertson, J. Microscopy 144 (1986) 229.
[18] M.M.J. Treacy, A. Howie and C.J. Wilson, Phil. Mag. A38 (1978) 569.
[19] M.M.J. Treacy, in: Scanning Electron Microscopy/1981, Ed. O. Johari (SEM, AMF O'Hare, IL, 1981) p. 185.
[20] S.J. Pennycook, J. Microscopy 124 (1981) 15.
[21] S.J. Pennycook, A. Howie, M.D. Shannon and R. Whyman, J. Mol. Catalysis 20 (1983) 345.
[22] M.M.J. Treacy and S.B. Rice, J. Microscopy, in press.
[23] S.J. Pennycook and J. Narayan, Appl. Phys. Letters 45 (1984) 385.
[24] P.A. Doyle and P.S. Turner, Acta Cryst. A24 (1968) 390.
[25] H. Fleischmann, Z. Naturforsch. 15a (1960) 1090.
[26] E.P. Fogarassy, D.H. Lowndes, J. Narayan and C.W. White, J. Appl. Phys. 58 (1985) 2167.
[27] J.S. Williams and R.G. Elliman, Appl. Phys. Letters 40 (1982) 266.
[28] E. Nygren, J.S. Williams, A. Pogany, R.G. Elliman, G.L. Olson and J.C. McCallum, Mater. Res. Soc. Symp. Proc. 74 (1987) 307.
[29] S.J. Pennycook, R.J. Culbertson and S.D. Berger, Mater. Res. Soc. Symp. Proc. 100 (1988) 411.
[30] F.A. Nichols, Acta Met. 20 (1972) 207.
[31] J.Y. Tsao and P.S. Peercy, Phys. Rev. Letters 58 (1987) 2782.
[32] S.J. Pennycook, S.D. Berger and R.J. Culbertson, in: Microscopy of Semiconducting Materials 1987, Inst. Phys. Conf. 87, Eds. A.G. Cullis and P.D. Augustus (Inst. Phys., London–Bristol, 1987) p. 503.
[33] S.J. Pennycook, in: Proc. 46th Annual EMSA Meeting, Milwaukee, WI, 1988, Ed. G.W. Bailey (San Francisco Press, San Francisco, 1988) p. 614.
[34] C.R.M. Grosvenor, P.E. Batson, D.A. Smith and C. Wong, Phil. Mag. A 50 (1984) 409.
[35] O. Scherzer, J. Appl. Phys. 20 (1949) 20.
[36] M.G.R. Thomson, Optik 39 (1973) 15.
[37] J.M. Cowley, Ultramicroscopy 2 (1976) 3.
[38] A.V. Crewe, Rept. Progr. Phys. 43 (1980) 621.
[39] D.A. Kopf, Optik 59 (1981) 89.
[40] M. Scheinfein and M. Isaacson, J. Vacuum Sci. Technol. B4 (1986) 326.
[41] C. Mory, C. Colliex and J.M. Cowley, Ultramicroscopy 21 (1987) 171.
[42] S.J. Pennycook and L.A. Boatner, Nature 336 (1988) 565.
[43] E.J. Kirkland, R.F. Loane and J. Silcox, Ultramicroscopy 23 (1987) 77.
[44] J. Fertig and H. Rose, Optik 59 (1981) 407.
[45] S.J. Pennycook, Scanning Microscopy 2 (1988) 21.
[46] B. Domenges, M. Hervieu, C. Michel and B. Raveau, Europhys. Letters 4 (1987) 211.
[47] H.W. Zandbergen, R. Gronsky and G. Thomas, Phys. Status Solidi (a) 105 (1988) 207.